Materials Science and Engineering B 285 (2022) 115939

Contents lists available at ScienceDirect

Materials Science & Engineering B

journal homepage: www.elsevier.com/locate/mseb

Synergy effect of temperature, electric and magnetic field on the depth structure of the FeRh/$BaTiO_3$ composite multiferroic

Attila Lengyel [a,*], Gábor Bazsó [a], Aleksandr I. Chumakov [b], Dénes L. Nagy [a], Gergő Hegedűs [a], Dimitrios Bessas [b], Zsolt E. Horváth [c], Norbert M. Nemes [d], Maria A. Gracheva [e], Edit Szilágyi [a], Szilárd Sajti [a], Dániel G. Merkel [a,c]

[a] Wigner Research Centre for Physics, P.O.B. 49, 1525 Budapest, Hungary
[b] ESRF – The European Synchrotron Radiation Facility, 71, Avenue des Martyrs, 38043 Grenoble, France
[c] Centre for Energy Research, P.O.B. 49, 1525 Budapest, Hungary
[d] GFMC, Departamento de Física de Materiales, Universidad Complutense de Madrid, E-28040 Madrid, Spain
[e] Institute of Chemistry, Eötvös Loránd University, Pázmány Péter sétány 1/A, 1117 Budapest, Hungary

ARTICLE INFO

Keywords:
FeRh
$BaTiO_3$
Multiferroic
Phase transition
Depth structure
Nuclear resonance scattering

ABSTRACT

FeRh based composite multiferroic materials have attracted great scientific interest due to their wide variety of possible applications in future nano device technology. In the recent work, a comprehensive study on the depth dependence of the metamagnetic phase transition in FeRh/$BaTiO_3$ heterostructure is reported by means of single or combined external stimulus such as heat, magnetic or electric field. Grazing-incidence nuclear scattering experiments revealed significant discrepancies in the mechanism of the antiferromagnetic/ferromagnetic reordering induced by the different effects, with distinguished role of both upper and lower interfaces.

1. Introduction

Due to the enormous increase of the world's energy consumption [1,2], the development of new, highly optimized and energy efficient devices are indispensable to maintain [3]. Composite multiferroics [4,5] are among the few novel materials that can be used to increase the efficiency of devices based on the principles of spintronics [6,7,8], magnetic switching [9,10,11], magnetic refrigeration [12,13,14,15], biomechanical energy harvesting [16,17,18], giant magnetoresistance [19,20,21] and photovoltaics [22,23,24].

The iron rhodium alloy is one of the most promising component of the composite multiferroic systems, due to its technologically exploitable mechanical and magnetic properties [25]. The equiatomic FeRh with a CsCl-type bcc-based B2 crystal structure [26] (see also Fig. 1 of ref. [27]) has a temperature-induced, fully reversible, *antiferromagnetic* (AFM) ↔ *ferromagnetic* (FM) phase transition in the operating temperature range of modern electronic devices [28,29,30]. The variation of the magnetic order is accompanied by the change of magnetic moments of the iron and rhodium atoms [31] and alters the electrical resistivity as well [32]. During the phase transition, about 1 % change in the lattice parameter was reported [33,34]. By reversing this phenomenon, mechanical compression can be used to trigger the FM-to-AFM magnetic phase transition of the alloy [35,36,37].

In order to create a composite multiferroic system, FeRh thin films are often coupled with piezoelectric materials, mostly $BaTiO_3$ (BTO) ceramics [25,37]. The epitaxial coupling between the crystal structures allows the alternation of the magnetic order of the alloy with external electric field through the piezoelectric effect [25,38,39,40,41].

The optimal utilization of the FeRh/BTO multiferroic requires the in-depth knowledge of magnetic configuration induced by technologically important effects, such as heat, magnetic and electric fields. However, the lateral AFM / FM structure has been thoroughly explored by various microscopy techniques [42,43,44,45,46], only a handful studies [47,48,49,50] described the depth-dependent AFM / FM phase structure in FeRh thin film, and no studies at all were devoted to the investigation of the magnetic depth profile triggered by joint effect of heat, magnetic or electric fields.

Here we report a comprehensive depth-resolved analysis of the AFM ↔ FM metamagnetic phase transition of the FeRh alloy in the composite multiferroic FeRh/$BaTiO_3$. By applying various temperature on the sample, we found permanent FM ordering in the vicinity of the upper and lower interfaces of the FeRh film, while continuous and

* Corresponding author.
E-mail address: lengyel.attila@wigner.hu (A. Lengyel).

https://doi.org/10.1016/j.mseb.2022.115939
Received 3 January 2022; Received in revised form 24 June 2022; Accepted 9 August 2022
Available online 21 August 2022

homogeneous AFM / FM phase transition could be observed in the middle region. The cumulative effect of magnetic field and temperature, altered the maximum achievable AFM fraction in correlation with the strength of the magnetic field. In contrast, the applied electric field combined with heating induced the magnetic phase transition with a rapid bottom-to-up orientation as soon as the voltage exceeded a threshold defined by the temperature of the alloy. Finally, we also demonstrated that the volume, where the electric field can induce the phase transition is adjustable by changing the temperature and external magnetic field.

The FeRh layer was deposited by molecular beam epitaxy (MBE) on the BTO substrate. Its atomic composition was specified by Rutherford backscattering spectrometry (RBS). The overall crystal structure and lattice parameters of the alloy were determined by X-ray diffractometry (XRD), while the thickness of the film was measured by X-ray reflectometry (XRR). The magnetic properties of the alloy were calculated from vibrating sample magnetometry (VSM) data and the iron micro-environments were determined by conversion electron Mössbauer spectroscopy (CEMS). Finally, the depth profile of the FeRh was investigated by grazing-incidence nuclear resonance scattering (GI-NRS).

2. Experimental

2.1. Sample preparation

The 5 mm × 5 mm × 1 mm $BaTiO_3$(1 0 0) substrate was purchased from Alineason Materials Technology GmbH. Prior to the FeRh deposition, it was cleaned in ultrasonic ethanol bath, followed by an 873 K bake out for 1800 s under ultra-high vacuum conditions. The ^{57}FeRh film of 18.0 nm nominal thickness was deposited on the BTO substrate using the MBE apparatus in the Wigner Research Centre for Physics (Wigner RCP). The ^{nat}Rh was evaporated from electron gun at growth rate of 0,0276 Å/s, while the ^{57}Fe was deposited from effusion cell at growth rate of 0,0154 Å/s, corresponding to the equiatomic composition. The temperature of the substrate was kept at 903 K while the pressure in the growing chamber never exceeded 3.7×10^{-8} mbar. The quality of the epitaxial growth was justified by in-situ reflection high-energy electron diffractometry (RHEED) shown in the **supplementary material**. At the end a 20 nm thick gold layer was deposited on the non-polished side of the BTO substrate for electric contact.

2.2. Characterization methods

2.2.1. Rutherford backscattering spectrometry

The RBS measurement (see **supplementary material**) of the ^{57}FeRh layer was performed using 2 MeV $^4He^+$ ion beam obtained from the 5 MV Van de Graaff accelerator of the Wigner RCP. The beam was collimated to the necessary dimensions of 0.5 × 0.5 mm^2 with two sets of four-sector slits. The measurements were performed with an ORTEC ruggedized partially depleted silicon radiation detector of a solid angle of 4.754 msr mounted at a scattering angle of 165° and at tilt angles 7° and 60°. The tilt angle 7° rather than perpendicular incidence was chosen and the sample was continuously rotated during the measurement around the azimuth axis to avoid channeling effects in the substrate. The measurement with 60° tilt angle was necessary since only taking spectra at two different tilt angles assured to make a distinction between the cases that an attenuated signal came from a lower-mass nucleus close to the surface or from a heavier nucleus in a deeper region of the thin film (mass-depth-ambiguity). The dose of the measurement was 4 μC. The ion current typically of 8 nA was measured by a transmission Faraday cup [51]. To reduce the surface contamination, liquid N_2 trap was used. The pressure in the scattering chamber was about 2.5×10^{-6} mbar during the experiments. The RBS data were evaluated by the RBX code [52].

2.2.2. X-ray diffractometry

XRD experiment was carried out at the Centre for Energy Research using a D8 Discover (Bruker AXS, Karlsruhe, Germany) diffractometer. Cu Kα radiation (λ = 1.5418 Å) was used for the measurement. To decrease beam divergence and to improve the parallelism of the beam, 1 mm slits were used at the source and the detector. Furthermore, a 90° rotated Soller slit was installed between the sample and the detector-side slit. At last, a secondary monochromator was used at the detector side, to achieve better signal-to-noise ratio. For the evaluation of the XRD results, the Diffrac.EVA [53] program was used. The XRD spectrum is shown in **supplementary material**.

2.2.3. Conversion electron Mössbauer spectroscopy

CEMS measurement was performed at the Wigner RCP using a conventional WissEl/DMSPCA Mössbauer spectrometer operated in sinusoidal drive mode at 16 Hz drive frequency. The activity of the ^{57}Co(Rh) single-line Mössbauer source was 621 MBq at the time of the measurement. The resonant conversion electrons were detected with a home-made gas-flow single-wire proportional counter of 1 mm distance

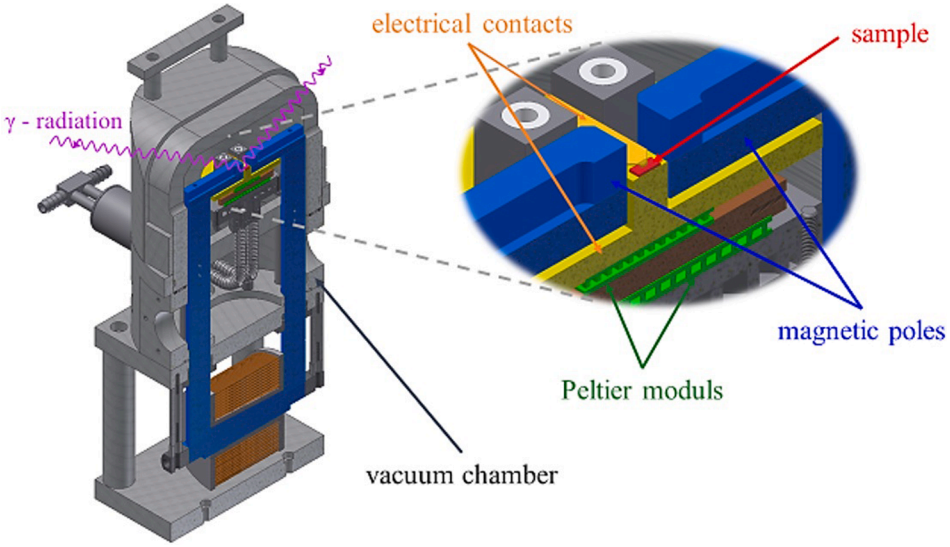

Fig. 1. Sketch of the sample holder designed for the GI-NRS experiment.

between sample and anode wire, working with a mixture of 96 % v/v He and 4 % v/v CH_4 gas at bias voltage 884 V. The distance between the source and the sample was 53 mm. Both source and sample were kept at room temperature. The spectrum was evaluated using the MossWinn 4 code [54].

2.2.4. Grazing-incidence nuclear resonance scattering and X-ray reflectometry

GI-NRS and XRR experiments were carried out at the Nuclear Resonance beamline [55] ID18 of the European Synchrotron Radiation Facility. The measurements were performed in 4 bunch mode at 14.414 keV, the energy corresponding to the 1/2 ↔ 3/2 nuclear transition of ^{57}Fe, with a beam of 0.5 meV energy bandpass. The beam was focused by a Kirkpatrick-Baez mirror system both horizontally and vertically to 20 μm and 8.7 μm, respectively. The sample was mounted in a custom-built vacuum chamber (Fig. 1) that allowed temperature (273 K – 400 K) control and adjustable voltage (0 V – 200 V) and magnetic field (0 mT – 150 mT) to be applied on the sample during the measurements. The GI-NRS quantum-beat patterns and XRR reflectograms were analyzed using the in-house (Wigner RCP) developed FitSuite program [56].

The GI-NRS measurements were carried out in four parts. At first, no external electric or magnetic field was applied. The temperature of the sample was raised directly to 394 K, then it was gradually lowered to 299 K, meanwhile GI-NRS quantum-beat patterns were recorded at three different grazing angles (3.49 mrad, 4.19 mrad and 4.71 mrad), at each temperature step (cooling phase). After the last 299 K measurement, the temperature of the sample was gradually raised back to 394 K, with similar measurements as in the cooling phase.

In the second part the same experimental protocol was used as before, except a 150 mT external magnetic field applied in the plane of the sample, parallel to the synchrotron beam.

Next, the temperature was set to 394 K; and voltage was applied step-by-step up to 100 V on the electric contacts (yellow parts in Fig. 1), where each stage GI-NRS curves recorded at the selected grazing angles. After the highest voltage measurements, the electric bias was released, and the sample was cooled down to the next temperature step, where the whole experimental procedure was repeated.

In the last, session, the previous (3rd) set of GI-NRS experiments were performed combined with 150 mT external magnetic field, applied as written previously.

2.2.5. Vibrating sample magnetometry

The magnetic moments were measured with a vibrating sample magnetometer from Quantum Design in a Physical Properties Measurement System equipped with a 9 T superconducting magnet (PPMS-9 T) at Complutense University of Madrid. All VSM measurements were performed in five orientations: four times in in-plane orientations [(1 0 0), (0 1 0), (1 1 0) and (−1 1 0)] and once in perpendicular direction (0 0 1), in the order listed. Magnetic hysteresis loops were measured in 10 K steps in the temperature range from 300 K to 400 K.

3. Results & discussion

From the evaluation of the RBS spectra, the ^{57}Fe and Rh atomic ratio was found to be 0.508 ± 0.018 and 0.492 ± 0.018, respectively. The XRD pattern verified the B2 structure of FeRh, while no other possible structure (e.g. to the paramagnetic A1 phase) could be identified, therefore the alloy can be considered structurally homogeneous. The lattice parameter was found to be (3.036 ± 0.001) Å, which is in close agreement with the B2 FeRh phase reported earlier [57]. XRR measurements resulted a uniform layer thickness of (16.8 ± 0.3) nm. High-level epitaxy between the $BaTiO_3$ substrate and the FeRh film was confirmed by RHEED. All the results of the characterization experiments (XRD, RBS, XRR and RHEED) are shown in **supplementary material**).

The iron microenvironments in the sample were determined by room temperature CEMS measurement (Fig. 2**a**). Based on previous results [43,58,59,60,61], the CEMS spectrum was fitted with four binomial distributions (BD) (only the effect of the next-neighbor atoms was taken into account), a sextet and two singlets. Both the ferromagnetic and the antiferromagnetic FeRh phases were described with three microenvironments apiece, 2 BD and a sextet for FM; and 2 BD and a singlet for AFM phase. Despite the equilibrium binary phase diagram of Fe and Rh exhibits only AFM phase at the present atomic concentration and room temperature [26], the FM phase is common in the case of thin films and is attributed to the small lattice mismatch between the BTO and the FeRh, as it was previously reported [47,49,62,63,64]. The last component; a very broad (unresolved) singlet, with intensity of 9 %; was associated to an unspecified oxide phase on the surface of the sample. The detailed description of the model used for the deconvolution of the CEMS spectrum can be found in the **supplementary material**.

For the GI-NRS model the overall layer structure and layer thickness were taken from the XRR measurements while the iron microenvironments from the CEMS results. To determine depth profile of the FeRh layer it was divided into ten sublayers (Fig. 2**b**). Each of these sublayers was uniformly set to 1.68 nm thick and were described as a homogeneous composition of all FeRh components from CEMS. During the analysis of the GI-NRS quantum-beat patterns, the Mössbauer parameters of the corresponding components were kept at the same values in each sublayer. As a result, the only parameters which could vary between the individual FeRh sublayers (at any given combination of temperature, electric field and magnetic field) were the relative amounts of the FM (X_{FM}) and AFM (X_{AFM}). However, X_{FM} was modeled as 1-X_{AFM} in each sublayer, therefore the only remaining independent parameter was X_{AFM} (in each layer), which is exclusively used to describe the alloys phase profile.

By simultaneously evaluating the three GI-NRS quantum-beat patterns recorded at different grazing angles at a given temperature and voltage, X_{AFM} values were determined individually in each FeRh sublayer based on similar principles that were described in refs. [65,66,67]. In Fig. 3, the calculated information depths belonging to each chosen grazing angle (in arbitrary units) as function of Mössbauer drive velocity is shown. It is apparent that at the resonance peaks the information

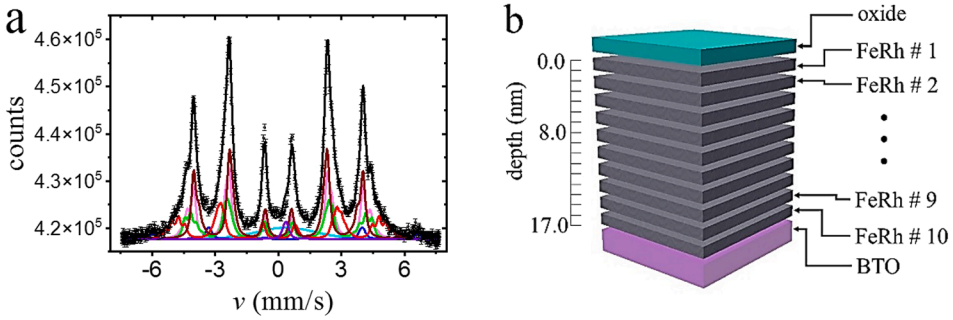

Fig. 2. (**a**) 294 K CEMS spectrum and (**b**) the arrangement of the sublayers in the GI-NRS model.

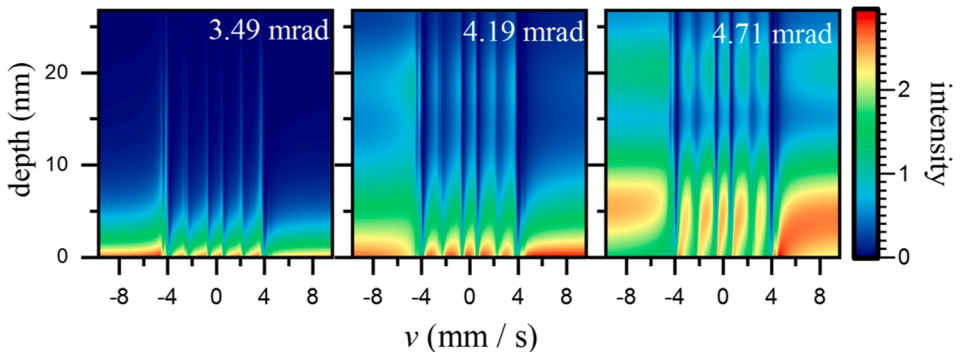

Fig. 3. Calculated information depths of the GI-NRS measurement at different grazing angles.

depth is quite shallow, however one has to keep in mind that in the measured quantum-beat patterns the whole broadened lines rather than only the peaks play role.

The calculated X_{AFM} values, along with their uncertainties, at each temperature (and for each magnetic/electric field combination), can be found in **Tables 3 to 15** in the **supplementary material**. The effect of different grazing on the quantum-beat patterns and the fitting of the above described model is illustrated on **Fig. 9** in **supplementary materials**.

3.1. Temperature effect on the depth profile of the phase transition

The determined X_{AFM} corresponding to each individual sublayer without applied magnetic- or electric fields is shown in a 2D intensity chart in the first column in Fig. 4, where the horizontal axis corresponds to the applied temperature, the vertical axis to the depth of the FeRh layer (sublayers), while the AFM ratio is presented by the color. There are contradictory results in the literature about the room temperature FM phases at the interfaces at. In ref. [43,44], mixed AFM and FM phases, in ref. [68,69], FM layer at the substrate and FeRh interface, in

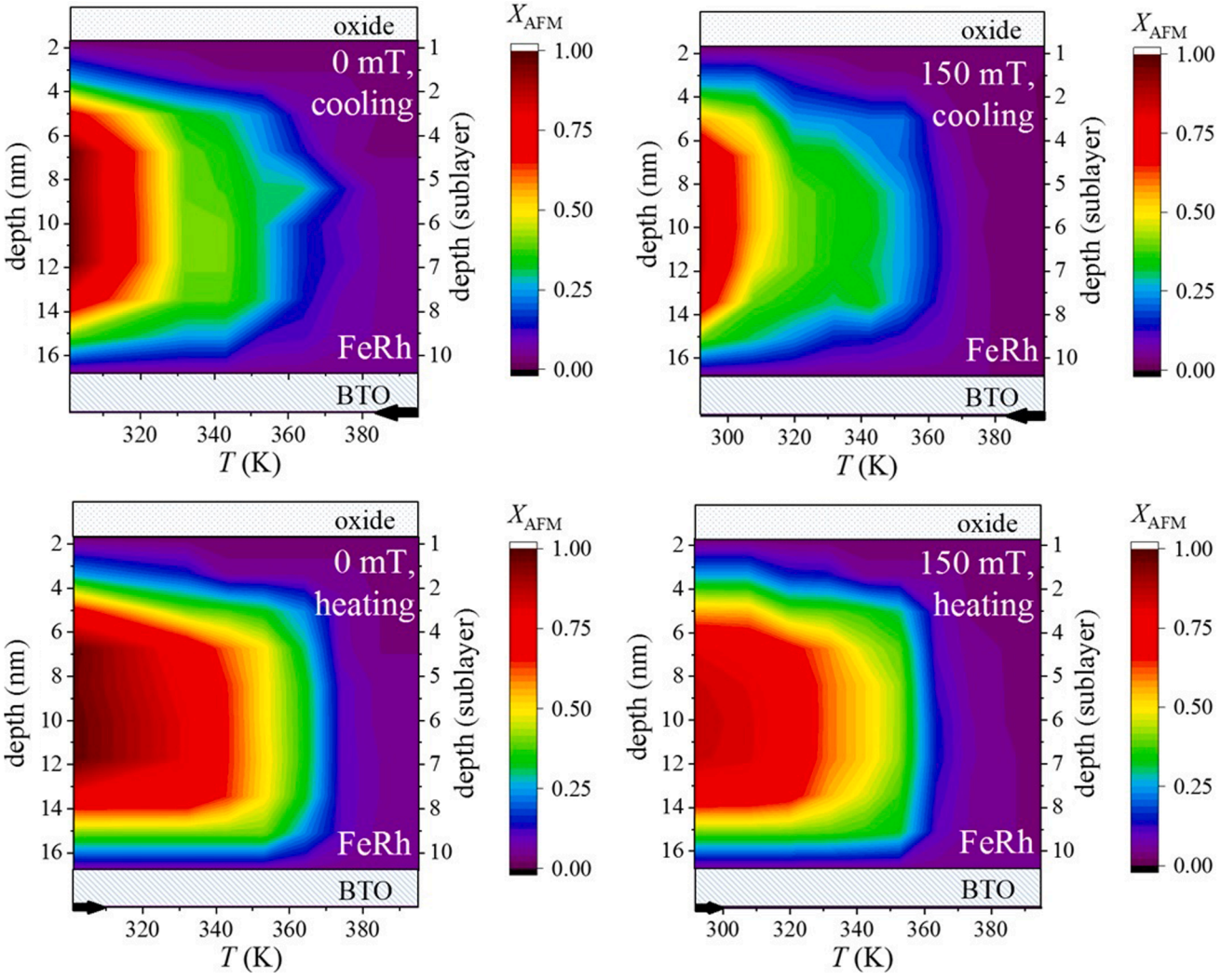

Fig. 4. The antiferromagnetic ratio (X_{AFM}) as a function of temperature with and without applied 150 mT magnetic field.

ref. [47] FM layer only at the upper interface and in ref. [49,50,70,71] FM layer at both upper and lower interface was identified. In our case, the experiments revealed the existence of FM order at both the upper and lower interfaces any temperature.

Despite, the impressing results of the latter works, the magnetic depth profile was either not determined or only at two or three selected temperatures, therefore the full mechanism of the metamagnetic transition cannot be reconstructed. A. S. Komlev and coworkers [47] suggested a model based on Bean-Rodbell and Kolmogorov-Johnson-Mehl-Avrami theory, stating that upon heating, the accumulation of the FM domains propagate from top to bottom. In case of heating (AFM-to-FM transition), we also found that the FM domain nucleation started at the upper interface followed by an increasing intensity ripening procedure (Fig. 4 bottom left). In the reverse course (FM-to-AFM transition), however, the AFM domains emerged at the middle region of the sample and superseded the FM regions towards the interfaces during the cooling process (Fig. 4 upper left). In both cases the middle part of the FeRh film ranging from #4 to #8 sublayer (from this point middle region) transformed practically homogenously (first column in Fig. 4). From a technology viewpoint, our results showed that the alloy layer always has to be at least 4 nm thick in the FeRh/BTO composite if temperature-induced AFM ↔ FM phase transition is required.

Upon heating, the overall magnetization in the sample was also followed by VSM measurements (Fig. 5**a**). At low temperatures magnetic hysteresis loops feature two coercive forces, which were associated to the FM and AFM regions in the sample. With increasing temperature a clear tendency of reduction of the coercive forces can be seen (Fig. 5**b**), accompanied by the enlargement of the saturation magnetization, from the initial ~ 400 emu/cm^3 to ~ 700 emu/cm^3. The full ferromagnetic characteristics of the hysteresis appears as high as 400 K, which can be the consequence of the tetragonal to cubic phase transformation of the epitaxial bound BTO. From VSM and GI-NRS results one can see that the magnetic reordering is continuous, no definite temperature threshold can be allocated for this procedure.

3.2. Synergy effect of magnetic field and temperature on the depth profile of the phase transition

S. Maat and coworkers [72] demonstrated that external magnetic field shifts the average spin structure towards FM ordering in FeRh thin film, however the depth dependence was not investigated. Therefore, we repeated the investigation of the metamagnetic transition with applied 150 mT magnetic field during the whole heating and cooling procedure. The in-depth variation of the antiferromagnetic ratio is shown in the second column in Fig. 4 and in detail in the **supplementary material**. The main features of the magnetic transitions didn't show significant deviation from the zero magnetic field case. The FM regions at both interfaces could be still observed at all temperatures and the FM and AFM nucleation followed similar behavior as described earlier. The main difference is that the applied magnetic field tries to preserve FM ordering (in agreement with ref 76), which means that the temperature of the AFM-to-FM transition shifts to lower values, while shifts to higher values in case of FM-to-AFM transition. In addition, the maximum accessible AFM ratio decreased from 98 % to 85 %.

3.3. Synergy effect of electric field and temperature on the depth profile of the phase transition

It is well known, that if strain is introduced to the crystal lattice of FeRh, its metamagnetic transition can be triggered [35,36,37,73], however the direct evidence of the depth-dependent magnetic processes is still unprecedented. For this reason, the effect of electric field on the magnetic depth profile was investigated during the FM-to-AFM transition in the cooling phase. In Fig. 6 the in-depth ratios of the antiferromagnetic domains are shown as a function of temperature in case of 0 V, 30 V, 60 V and 100 V applied voltage (the corresponding data for the individual sublayers are shown in the **supplementary material**). In contrast to the fully temperature driven (and magnetic field assisted) metamagnetic transition, it can be seen, that the AFM nucleation starts at the FeRh/BTO interface, caused by the piezoelectricity induced strain in the BTO substrate. It seems, that this strain effect at a given temperature exhibits a threshold thickness (relative to the lower interface) within the spin reorientation is approximately the same and above the effect decays continuously.

Above 390 K, the FM phase was found energetically stable even when the highest voltage was applied. By analyzing the 2D charts in Fig. 6 one can see that the exact range of electric field strength that triggers the phase transition is determined by the temperature. In the case of 60 V and 100 V applied voltage and in the lower half of the sample, an abrupt jump in the AFM ratio occurred in a narrow temperature range around 360 K and 370 K, respectively. In case of 30 V, this rise undergoes through a much broader temperature range. In the upper half of the FeRh film, closer to the oxide, the FM / AFM transition was found to be more restrained at all voltages

Our results suggest that the expected devices for this multiferroic coupling have an ideal operating temperature of 342 K and a FeRh layer thickness of less than 9 nm. However, for exclusively voltage controlled phase transition, the FeRh layer should be no thicker than 5 nm.

3.4. Combined effect of temperature, external magnetic- and -electric fields on the depth profile of the phase transition

Up until now, the joint effect of temperature, electric and magnetic field on the metamagnetic transition of FeRh was not presented. In order to investigate the synergy of these effects GI-NRS measurements were carried with simultaneously applied 150 mT external magnetic field and 100 V voltage after the sample was cooled down to a certain temperature from the initial 394 K. The full combination of the applied effects on the

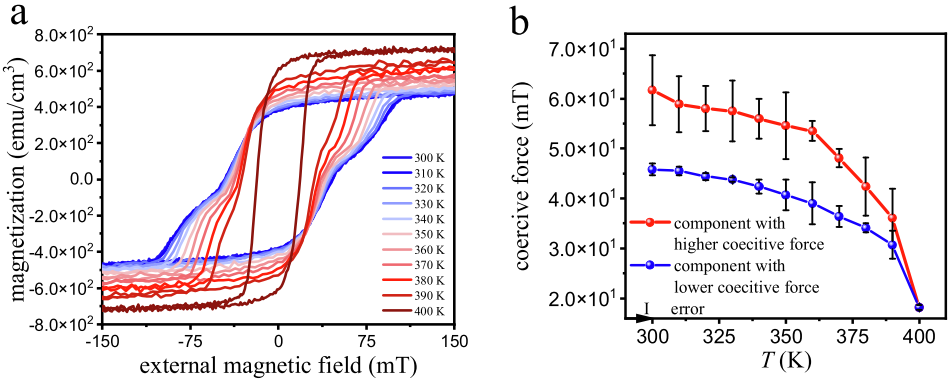

Fig. 5. (**a**) Magnetization at (0 1 0) direction and (**b**) coercive forces as a function of magnetic field and temperature in the FeRh/BTO composite.

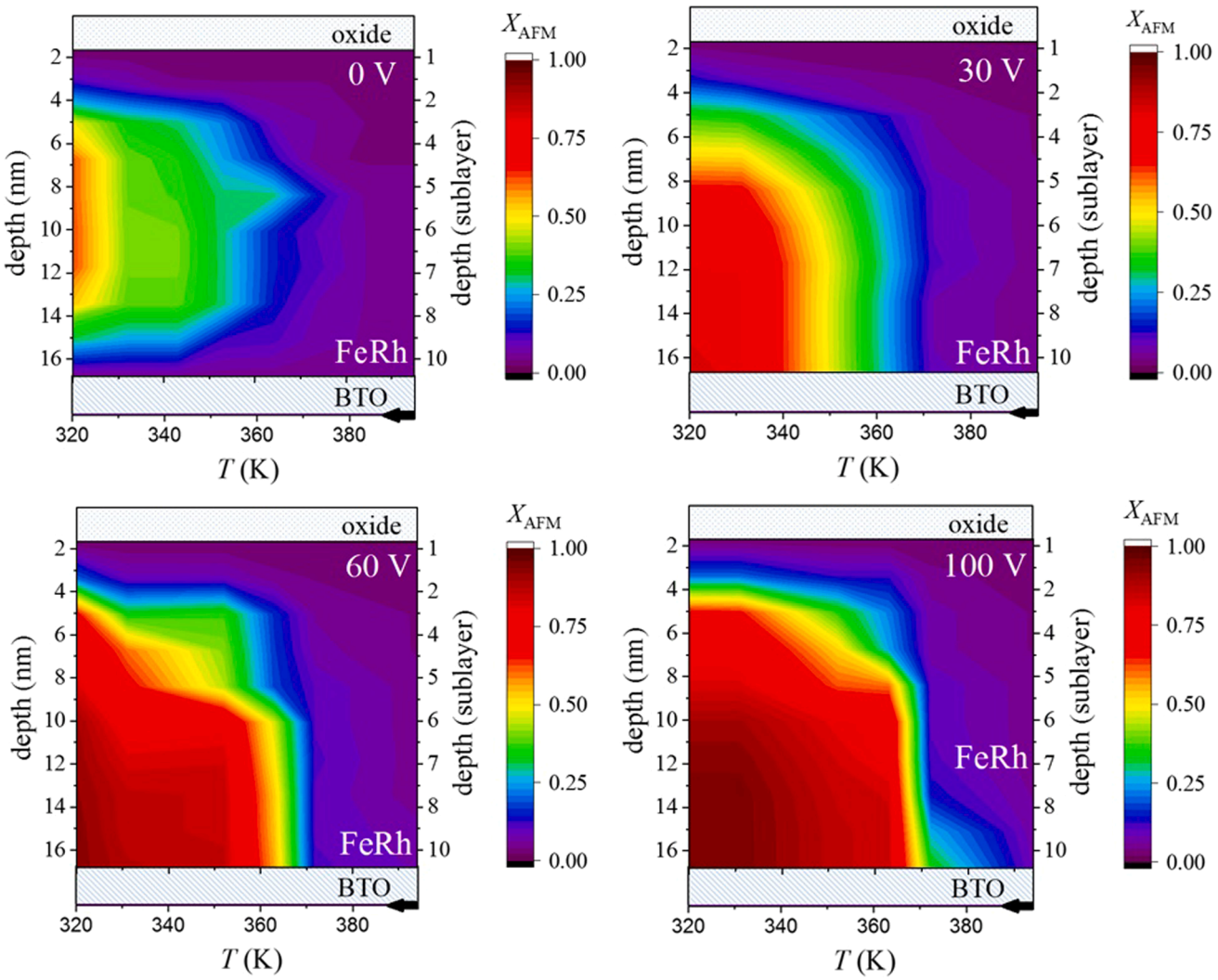

Fig. 6. X_{AFM} as a function of temperature with various voltages during cooling phase, without applied magnetic field.

in-depth magnetic ordering is shown in Fig. 7 at 331 K, 352 K and at 372 K. A strong inhibitory effect of magnetic field on the AFM nucleation was observed, which means, that the external magnetic field not only enhances the effect of heat (as it was shown in chapter 3.2), but immensely reduces the effect of the electric field. However, the magnetic field itself had no effect at the vicinity of the substrate, combined with the electric field it has a significant contribution to the formed magnetic phase. It was shown that the relative strength of heat, electric and magnetic fields is not homogeneous throughout the FeRh layer; at the FeRh/BTO interface the effect of the electric field is the strongest. Away from the interface, the AFM / FM phase ratio is governed by the balance of temperature, magnetic and electric field, and further away the effect of electric field is negligible. Within the given experimental conditions, the effect of temperature extends to 13 nm from the substrate at 331 K without external magnetic field, but only to 9 nm at 352 K with 0 mT external magnetic field or at 331 K with 150 mT (Fig. 7). Therefore, the FeRh thickness where the external electric field could trigger the FM-to-AFM phase transition, was determined by the combination of temperature and the strength of external magnetic field.

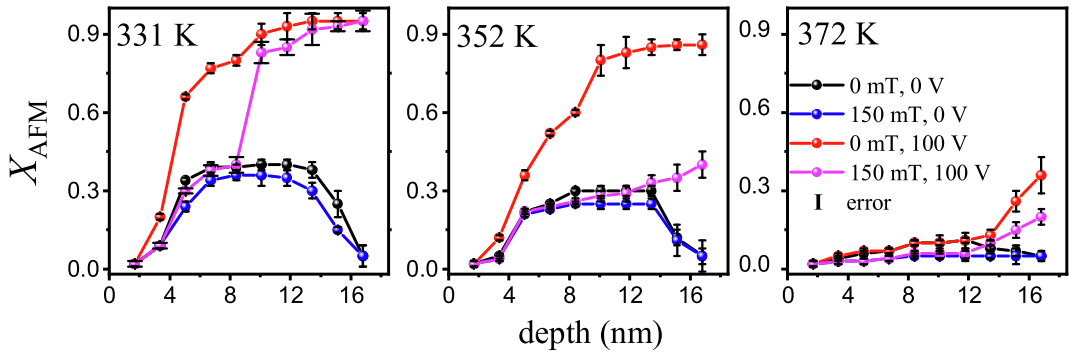

Fig. 7. X_{AFM} as a function of temperature, external electric and magnetic fields in the FeRh/BTO composite; during cooling phases.

4. Conclusion

In this study the depth-dependent effects of temperature, external magnetic and electric fields on the AFM / FM phase ratio of the alloy in the FeRh/BTO multiferroic were determined by GI-NRS measurements.

It was found that the FM phase at the top and bottom interfaces of the FeRh layer never transformed into the AFM phase by temperature alone, regardless of whether magnetic field is present or not. In case temperature induced AFM-to-FM transition we found that the FM domain nucleation started at the upper interface followed by an increasing intensity ripening procedure. On the contrary, in the cooling phase (FM-to-AFM transition), the AFM domains emerged at the middle region of the sample and superseded the FM regions towards the interfaces during the cooling process.

When external magnetic field was applied, a clear temperature shift of the metamagnetic phase transition was evidenced in a way, that the system preserves FM ordering. The maximum ratio of the AFM phase decreased from 98 % to 85 %.

In case of utilization of external electric field without magnetic field, the AFM nucleation started at the FeRh/BTO interface, hence even the lowest FM sublayer could be converted into AFM phase. The induced FM-to-AFM transition was found to be homogenous up to a certain layer thickness (relative to the bottom interface) but above, the influence of the electric field reduced substantially

When the synergy of all effect was investigated, a strong inhibitory effect of magnetic field on the AFM nucleation was observed, which manifested in the reduction of effect of the electric field. The strength of this reduction was found to be temperature and depth dependent.

It was shown that the relative strength of heat, electric and magnetic fields is not homogeneous throughout the FeRh layer, therefore to achieve the application compatible in-depth magnetic configuration, the proper balance of these effects is extremely important.

CRediT authorship contribution statement

Attila Lengyel: Investigation, Data curation, Methodology, Writing – original draft. **Gábor Bazsó:** Investigation. **Aleksandr I. Chumakov:** Investigation, Resources. **Dénes L. Nagy:** Investigation, Methodology, Writing – review & editing. **Gergő Hegedűs:** Resources. **Dimitrios Bessas:** Resources. **Zsolt E. Horváth:** Investigation. **Norbert M. Nemes:** Investigation. **Maria A. Gracheva:** Investigation, Writing – review & editing. **Edit Szilágyi:** Investigation. **Szilárd Sajti:** . **Dániel G. Merkel:** Conceptualization, Supervision, Investigation, Data curation, Methodology, Funding acquisition, Writing – review & editing.

Declaration of Competing Interest

The authors declare that they have no known competing financial interests or personal relationships that could have appeared to influence the work reported in this paper.

Data availability

The data that indicated the above-described results are available in the CONCORDA repository under entry: https://science-data.hu/dataset.xhtml?persistentId=doi:10.5072/FK2/5VJBZQ.

Acknowledgements

We acknowledge the European Synchrotron Radiation Facility for provision of synchrotron radiation resources at the beamline ID18 and we thank Mr. J.-P. Celse for technical assistance during the beamtime.

This research did not receive any specific grant from funding agencies in the public, commercial, or not-for-profit sectors.

Appendix A. Supplementary material

Supplementary data to this article can be found online at https://doi.org/10.1016/j.mseb.2022.115939.

References

[1] J. Puebla, J. Kim, K. Kondou, Y. Otani, Spintronic devices for energy-efficient data storage and energy harvesting, Commun. Mater. 1 (2020) 24, https://doi.org/10.1038/s43246-020-0022-5.
[2] https://www.iea.org/data-and-statistics/charts/global-electricity-demand-by-scenario-2010-2030.
[3] E. Inshakova, A. Inshakova, A. Goncharov, Engineered nanomaterials for energy sector: market trends, modern applications and future prospects, IOP Conf. Ser.: Mater. Sci. Eng. 971 (3) (2020) 032031.
[4] H. Ohno, D. Chiba, F. Matsukura, T. Omiya, E. Abe, T. Dietl, Y. Ohne, K. Ohtani, Electric-field control of ferromagnetism, Nature 408 (6815) (2000) 944–946, https://doi.org/10.1038/35050040.
[5] R. Ramesh, N.A. Spaldin, Multiferroics: progress and prospects in thin films, Nat. Mater. 6 (1) (2007) 21–29, https://doi.org/10.1038/nmat1805.
[6] M. Trassin, Low energy consumption spintronics using multiferroic heterostructures, J. Phys.: Condens. Matter 28 (3) (2015), 033001, https://doi.org/10.1088/0953-8984/28/3/033001.
[7] Z. Feng, H. Yan, Z. Liu, Electric-Field Control of Magnetic Order: From FeRh to Topological Antiferromagnetic Spintronics, Adv. Electron. Mater. 5 (1) (2019) 1800466.
[8] S.-J. Chang, M.-H. Chung, M.-Y. Kao, S.-F. Lee, Y.-H. Yu, C.-C. Kaun, T. Nakamura, N. Sasabe, S.-J. Chu, Y.-C. Tseng, $GdFe_{0.8}Ni_{0.2}O_3$: a multiferroic material for low-power spintronic devices with high storage capacity, ACS Appl. Mater. Interfaces 11 (34) (2019) 31562–31572.
[9] I. Fina, A. Quintana, X. Martí, F. Sánchez, M. Foerster, L. Aballe, J. Sort, J. Fontcuberta, Reversible and magnetically unassisted voltage-driven switching of magnetization in FeRh/PMN-PT, Appl. Phys. Lett. 113 (15) (2018), 152901, https://doi.org/10.1063/1.5040184.
[10] F. Matsukura, Y. Tokura, H. Ohno, Control of magnetism by electric fields, Nat. Nanotechnol. 10 (3) (2015) 209–220, https://doi.org/10.1038/nnano.2015.22.
[11] X. Tang, J. Shang, Y. Gu, A. Du, L. Kou, Reversible Gas Capture by Ferroelectric Switch and 2D Molecule Multiferroics in In_2Se_3 Monolayer, J. Mater. Chem. A 8 (15) (2020) 7331–7338, https://doi.org/10.1039/D0TA00854K.
[12] M.L. Arreguín-Hernández, C.F. Sánchez-Valdés, J.L.S. Llamazares, D. Ríos-Jara, V. K. Pecharsky, M.I. Blinov, V.N. Prudnikov, B.B. Kovalev, V.I. Zverev, A.M. Tishin, Magnetoelastic transition and magnetocaloric effect in induction melted $Fe_{100-x}Rh_x$ bulk alloys with x = 50, 51, J. Alloy. Compd. 871 (2021), 159586, https://doi.org/10.1016/j.jallcom.2021.159586.
[13] R. Barua, F. Jiménez-Villacorta, L.H. Lewis, Towards tailoring the magnetocaloric response in FeRh-based ternary compounds, J. Appl. Phys. 115 (17) (2014) 17A903, https://doi.org/10.1063/1.4854975.
[14] I.A. Starkov, A.S. Starkov, On the thermodynamic foundations of solid-state cooler based on multiferroic materials, Int. J. Refrig 37 (2014) 249–256, https://doi.org/10.1016/j.ijrefrig.2013.08.006.
[15] M. Alam, S. Ghosh, K. Mandal, Magnetic and magnetocaloric properties in double perovskite multiferroic $_Y2NiMn_O6$ nanoparticle, in: DAE Solid State Physics Symposium 2019, 2020, https://doi.org/10.1063/5.0017702.
[16] H. Wua, A. Tatarenko, M.I. Bichurin, Y. Wanga, A multiferroic module for biomechanical energy harvesting, Nano Energy 83 (2021), 105777, https://doi.org/10.1016/j.nanoen.2021.105777.
[17] B.K. Panigrahi, D. Sitikantha, A. Bhuyan, H.S. Panda, K. Mohanta, Dielectric and ferroelectric properties of PVDF thin film for biomechanical energy harvesting, Mater. Today:. Proc. 41 (2) (2021) 335–339, https://doi.org/10.1016/j.matpr.2020.09.339.
[18] H. Wu, A. Tatarenko, M.I. Bichurin, Y. Wang, A multiferroic module for biomechanical energy harvesting, Nano Energy 83 (2021), 105777, https://doi.org/10.1016/j.nanoen.2021.105777.
[19] N.A. Zarkevich, V.I. Zverev, Viable Materials with a Giant Magnetocaloric Effect, Crystals 10 (9) (2020) 815, https://doi.org/10.3390/cryst10090815.
[20] J. Van Driel, R. Coehoorn, G.J. Strijkers, E. Brück, F.R. de Boer, Compositional dependence of the giant magnetoresistance in Fe_xRh_{1-x} thin films, J. Appl. Phys. 85 (2) (1999) 1026–1036, https://doi.org/10.1063/1.369224.
[21] I. Suzuki, T. Naito, M. Itoh, T. Sato, T., Taniyama, Clear correspondence between magnetoresistance and magnetization of epitaxially grown ordered FeRh thin films., J. Appl. Phys., 109(7), 07C717 (2011), doi: https://doi.org/10.1063/1.3556754.
[22] N.A. Spaldin, Multiferroics beyond electric-field control of magnetism, Proc. R. Soc. A: Math. Phys. Eng. Sci. 476 (2233) (2020) 20190542, https://doi.org/10.1098/rspa.2019.0542.
[23] G. Zhang, H. Wu, G. Li, Q. Huang, C. Yang, F. Huang, F. Liao, J. Lin, New high Tc multiferroics $KBiFe_2O_5$ with narrow band gap and promising photovoltaic effect, Sci. Rep. 3 (2013) 1265, https://doi.org/10.1038/srep01265.
[24] C.M. Hung, C.S. Tu, W.D. Yen, L.S. Jou, M.D. Jiang, V.H. Schmidt, Photovoltaic phenomena in $BiFeO_3$ multiferroic ceramics, J. Appl. Phys. 111 (7) (2012) 07D912, https://doi.org/10.1063/1.3675984.
[25] R.O. Cherifi, V. Ivanovskaya, L.C. Phillips, A. Zobelli, I.C. Infante, E. Jacquet, V. Garcia, S. Fusil, P.R. Briddon, N. Guiblin, A. Mougin, A.A. Unal, F. Kronast, S. Valencia, B. Dkhil, A. Barthel, M. Bibes, Electric-field control of magnetic order

above room temperature, Nat. Mater. 13 (4) (2014) 345–351, https://doi.org/10.1038/nmat3870.
[26] L. Swartzendruber, The Fe-Rh (Iron-Rhodium) System, Bull. Alloy Phase Diagrams 5 (5) (1984) 456–462.
[27] H. Kumar, D.R. Cornejo, S.L. Morelhao, S. Kycia, I.M. Montellano, N.R. Álvarez, G. Alejandro, A. Butera, Strain effects on the magnetic order of epitaxial FeRh thin films, J. Appl. Phys. 124 (8) (2018) 085306.
[28] M. Fallot, R. Hocart, Sur l'apparation du ferromagnetisme par elevation de temperature dans des alliages de fer et de rhodium, Rev. Sci. 77 (1939) 498–501.
[29] J.S. Kouvel, C.C. Hartelius, Anomalous Magnetic Moments and Transformations in the Ordered Alloy FeRh, J. Appl. Phys. 33 (3) (1962) 1343–1344, https://doi.org/10.1063/1.1728721.
[30] L. Muldawer, F. deBergevin, Antiferromagnetic-Ferromagnetic Transformation in FeRh, J. Chem. Phys. 35 (5) (1961) 1904–1905, https://doi.org/10.1063/1.1732175.
[31] G. Shirane, R. Nathans, C.W. Chen, Magnetic Moments and Unpaired Spin Densities in the Fe-Rh Alloys, Phys. Rev. 134, A1547-A1553 **(1964)**.
[32] S. Yuasa, T. Akiyama, H. Miyajima, Y. Otani, Change in the Resistivity of bcc and bct FeRh Alloys at First-Order Magnetic Phase Transitions, J. Phys. Soc. Jpn. 64 (10) (1995) 3978–3985, https://doi.org/10.1143/jpsj.64.3978.
[33] E.F. Bertaut, A. Delapalme, F. Forrat, G. Roult, F. De Bergevin, R. Pauthenet, Magnetic Structure Work at the Nuclear Center of Grenoble, J. Appl. Phys. 33 (3) (1962) 1123–1124, https://doi.org/10.1063/1.1728627.
[34] F. Bertaut, F. de Bergevin, G. Roult, Magnetisme-etude par diffraction neutronique de $Fe_{0,47}Rh_{0,53}$, Compt. Rend. 256 (1963) 1668.
[35] S. Yuasa, H. Miyajima, Y. Otani, Magneto-Volume and Tetragonal Elongation Effects on Magnetic Phase Transitions of Body-Centered Tetragonal $FeRh_{1-x}Pt_x$, J. Phys. Soc. Jpn. 63 (8) (1994) 3129–3144, https://doi.org/10.1143/jpsj.63.3129.
[36] A.I. Zakharov, A.M. Kadomtseva, R.Z. Levitin, E.G. Ponyatovskii, Magnetic and magnetoelastic properties of a metamagnetic Fe–Rh alloy, J. Exp. Theor. Phys. 46 (1964) 1348–1353.
[37] L. Phillips, R.O. Cherifi, V. Ivanovskaya, A. Zobelli, I.C. Infante, E. Jacquet, N. Guiblin, A.A. Ünal, F. Kronast, B. Dkhil, A. Barthélémy, M. Bibes, S. Valencia, Local electrical control of magnetic order and orientation by ferroelastic domain arrangements just above room temperature, Sci. Rep. 5 (2015) 10026, https://doi.org/10.1038/srep10026.
[38] J.T. Heron, D.G. Schlom, R. Ramesh, Electric field control of magnetism using $BiFeO_3$-based heterostructures, Appl. Phys. Rev. 1 (2) (2014), 021303, https://doi.org/10.1063/1.4870957.
[39] J. Chen, J. Ma, Y. Zhang, S. Bao, L. Wu, C. Liu, C.W. Nan, Strain modulated ferromagnetic to antiferromagnetic transition in FeRh/$BaTiO_3$ (001) heterostructures, J. Appl. Phys. 121 (19) (2017), 194101, https://doi.org/10.1063/1.4983361.
[40] L.H. Lewis, C.H. Marrows, S. Langridge, Coupled magnetic, structural, and electronic phase transitions in FeRh, J. Phys. D Appl. Phys. 49 (32) (2016), 323002, https://doi.org/10.1088/0022-3727/49/32/323002.
[41] A.A. Amirov, V.V. Rodionov, V. Komanicky, V. Latyshev, E.Y. Kaniukov, V. V. Rodionova, Magnetic phase transition and magnetoelectric coupling in FeRh film. Journal of Magnetism and Magnetic Materials, J. Magn. Magn. Mater. 479 (2019) 1, https://doi.org/10.1016/j.jmmm.2019.01.079.
[42] Y. Yokoyama, M. Usukura, S. Yuasa, Y. Suzuki, H. Miyajima, T. Katayama, "MFM observation of magnetic phase transitions in ordered FeRh systems, J. Magn. Magn. Mater. 177–181 (1998) 181–182, https://doi.org/10.1016/s0304-8853(97)00953-0.
[43] R.C. Temple, T.P. Almeida, J.R. Massey, K. Fallon, R. Lamb, S.A. Morley, F. Maccherozzi, S.S. Dhesi, D. McGrouther, S. McVitie, T.A. Moore, C.H. Marrows, Antiferromagnetic-ferromagnetic phase domain development in nanopatterned FeRh islands, Phys. Rev. Materials 2 (2018), 104406, https://doi.org/10.1103/PhysRevMaterials.2.104406.
[44] T.P. Almeida, R. Temple, J. Massey, K. Fallon, D. McGrouther, T. Moore, C. H. Marrows, S. McVitie, Quantitative TEM imaging of the magnetostructural and phase transitions in FeRh thin film systems, Sci. Rep. 7 (2017) 17835, https://doi.org/10.1038/s41598-017-18194-0.
[45] S.P. Bennett, A. Herklotz, C.D. Cress, A. Ievlev, C.M. Rouleau, I.I. Mazin, V. Lauter, Magnetic order multilayering in FeRh thin films by He-Ion irradiation, Mater. Res. Lett. 6 (1) (2017) 106–112, https://doi.org/10.1080/21663831.2017.1402098.
[46] D.G. Merkel, A. Lengyel, D.L. Nagy, A. Németh, Z.E. Horváth, C. Bogdán, M. A. Gracheva, G. Hegedűs, S. Sajti, G.Z. Radnóczi, E. Szilágyi, Reversible control of magnetism in FeRh thin films, Sci. Rep. 10 (1) (2020), https://doi.org/10.1038/s41598-020-70899-x.
[47] A.S. Komlev, D.Y. Karpenkov, D.A. Kiselev, T.S. Ilina, A. Chirkova, R.R. Gimaev, T. Usami, T. Taniyama, V.I. Zverev, N.S. Perov, Ferromagnetic phase nucleation and its growth evolution in FeRh thin films, J. Alloy. Compd. 874 (2021), 159924, https://doi.org/10.1016/j.jallcom.2021.159924.
[48] C. Gatel, B. Warot-Fonrose, N. Biziere, L.A. Rodríguez, D. Reyes, R. Cours, M. Castiella, M.J. Casanove, Inhomogeneous spatial distribution of the magnetic transition in an iron-rhodium thin film, Natur. Comm. 8 (2017) 15703, https://doi.org/10.1038/ncomms15703.
[49] C. Bull, C.W. Barton, W. Griggs, A. Caruana, C.J. Kinane, P.W. Nutter, T. Thomson, PNR study of the phase transition in FeRh thin films, APL Mater. 7 (10) (2019), 101117, https://doi.org/10.1063/1.5120622.
[50] W. Griggs, B. Eggert, M.O. Liedke, M. Butterling, A. Wagner, U. Kentsch, E. Hirschmann, M. Grimes, A.J. Caruana, C. Kinane, H. Wende, R. Bali, T. Thomson, T.,, Depth selective magnetic phase coexistence in FeRh thin films, APL Mater. 8, 12 (2020), 121103, https://doi.org/10.1063/5.0032130.
[51] F. Pászti, A. Manuaba, C. Hajdu, A.A. Melo, M. f., Da Silva, Current measurement on MeV energy ion beams, Nucl. Instrum. Methods Phys. Res., Sect. B 47 (2) (1990) 187–192, https://doi.org/10.1016/0168-583x(90)90028-s.
[52] E. Kótai, Computer methods for analysis and simulation of RBS and ERDA spectra, Nucl. Instrum. Methods Phys. Res., Sect. B 85 (1–4) (1994) 588–596, https://doi.org/10.1016/0168-583x(94)95888-2.
[53] https://www.bruker.com/en/products-and-solutions/diffractometers-and-scattering- systems/x-ray-diffractometers/diffrac-suite-software/diffrac-eva.html.
[54] Z. Klencsár, E. Kuzmann, A. Vértes, User-friendly software for Mössbauer spectrum analysis", J. Radioanal. Nucl. Chem. Art. 210 (1) (1996) 105–118, https://doi.org/10.1007/bf02055410.
[55] R. Rüffer, A.I. Chumakov, Nuclear Resonance Beamline at ESRF", Hyperfine Interact. 97–98 (1) (1996) 589–604, https://doi.org/10.1007/bf02150199.
[56] Sz. Sajti, H. Spiering, FitSuite. https://www.fs.kfki.hu.
[57] C. Le Graët, M.A. de Vries, M. McLaren, R.M.D. Brydson, M. Loving, D. Heiman, L. H. Lewis, C.H. Marrows, Sputter growth and characterization of metamagnetic B2-ordered FeRh epilayers, J. Visualized Experiments: JoVE 80 (2013), https://doi.org/10.3791/50603.
[58] I.A. Vincze, Campbell, Mössbauer measurements in iron based alloys with transition metals., J. Phys. F: Metal Phys, 3(3), 647-336 **(1973),** doi: https://doi.org/10.1088/0305-4608/3/3/023.
[59] G. Shirane, C.W. Chen, P.A. Flinn, R. Nathans, Mössbauer study of hyperfine fields and isomer shifts in the Fe-Rh alloys, Phys. Rev. 131 (1) (1963) 183–190.
[60] A. Błachowski, K. Ruebenbauer, J. Żukrowski, Spin- and charge density around Rh impurity in α-Fe studied by ^{57}Fe Mössbauer spectroscopy, J. Alloy. Compd. 477 (1–2) (2009) 4–7, https://doi.org/10.1016/j.jallcom.2008.10.013.
[61] M. Rosenberg, V. Kuncser, O. Crisan, A. Hernando, E. Navarro, G. Filoti, A Mössbauer spectroscopy and magnetic study of FeRh, J. Magn. Magn. Mater. 177–181 (1998) 135–136, https://doi.org/10.1016/s0304-8853(97)00662-8.
[62] I. Suzuki, T. Koike, M. Itoh, T. Taniyama, T. Sato, Stability of ferromagnetic state of epitaxially grown ordered FeRh thin films, J. Appl. Phys. 105 (7) (2009) 07E501, https://doi.org/10.1063/1.3054386.
[63] C. Baldasseroni, G.K. Pálsson, C. Bordel, S. Valencia, A.A. Unal, F. Kronast, S. Nemsak, C.S. Fadley, J.A. Borchers, B.B. Mranville, F. Hellman, Effect of capping material on interfacial ferromagnetism in FeRh thin films, J. Appl. Phys. 115 (4) (2014), 043919, https://doi.org/10.1063/1.4862961.
[64] J.R. Massey, R.C. Temple, T.P. Almeida, R. Lamb, N.A. Peters, R.P. Campion, R. Fan, D. McGrouther, S. McVitie, P. Steadmam, C.H. Marrows, Asymmetric magnetic relaxation behavior of domains and domain walls observed through the FeRh first-order metamagnetic phase transition, Phys. Rev. B 102 (14) (2020), https://doi.org/10.1103/physrevb.102.144304.
[65] W.A.A. Macedo, Depth-resolved studies of layered magnetic nanostructures using ^{57}Fe probe layers and Mössbauer spectroscopy, J. Magn. Magn. Mater. 368 (2014) 402–408, https://doi.org/10.1016/j.jmmm.2014.04.035.
[66] A.I. Chumakov, L. Niesen, D.L. Nagy, E.E. Alp, Nuclear resonant scattering of synchrotron radiation by multilayer structures, Hyperfine Interact. 123/124 (1/4) (1999) 427–454, https://doi.org/10.1023/a:1017028024642.
[67] D.L. Nagy, L. Bottyán, L. Deák, J. Dekoster, G. Langouche, V.G. Semenov, H. Spiering, E. Szilágyi, Synchrotron Mössbauer reflectometry in materials science., *Mössbauer Spectroscopy in Materials Science*, in: M. Miglierini, D. Petridis (Eds.), Mössbauer Spectroscopy in Materials Science, Springer Netherlands, Dordrecht, 1999, pp. 323–336.
[68] J. Hong, T. Yang, A.T. N'Diaye, J. Bokor, L. You, Effects of interface induced natural strains on magnetic properties of FeRh, Nanomaterials 9 (2019) 574, https://doi.org/10.3390/nano9040574.
[69] R. Fan, C.J. Kinane, T.R. Charlton, R. Dorner, M. Ali, M.A. de Vries, R.M. D. Brydson, C.H. Marrows, B.J. Hickey, D.A. Arena, B.K. Tanner, G. Nisbet, S. Langridge, Ferromagnetism at the interfaces of antiferromagnetic FeRh epilayers, Phys. Rev. B 82 (2010), 184418, https://doi.org/10.1103/PhysRevB.82.184418.
[70] C. Baldasseroni, G.K. Pálsson, C. Bordel, S. Valencia, A.A. Unal, F. Kronast, S. Nemsak, C.S. Fadley, J.A. Borchers, B.B. Maranville, F. Hellman, Effect of capping material on interfacial ferromagnetism in FeRh thin films, J. Appl. Phys. 115 (4) (2014) 043919.
[71] I. Fina, J. Fontcuberta, Strain and voltage control of magnetic and electric properties of FeRh films, J. Phys. D: Appl. Phys. 53 (2) (2020) 023002.
[72] S. Maat, J.U. Thiele, E.E. Fullerton, Temperature and field hysteresis of the antiferromagnetic-to-ferromagnetic phase transition in epitaxial FeRh films, Phys. Rev. B 72 (21) (2005), https://doi.org/10.1103/physrevb.72.214432.
[73] U. Aschauer, R. Braddell, S.A. Brechbühl, P.M. Derlet, N.A. Spaldin, Strain-induced structural instability in FeRh, Phys. Rev. B 94 (1) (2016), https://doi.org/10.1103/physrevb.94.014109.